Design and validation of reactant feeding control strategies for the solar-autothermal hybrid gasification of woody biomass

Axel Curcio, Sylvain Rodat, Valéry Vuillerme, Stéphane Abanades

Design and Validation of Reactant Feeding Control Strategies for the Solar-Autothermal Hybrid Gasification of Woody Biomass

Axel Curcio [1], Sylvain Rodat [1], Valéry Vuillerme [2], Stéphane Abanades [1 *]

[1] Processes, Materials and Solar Energy Laboratory, PROMES - CNRS,
7 rue du Four Solaire, 66120 Font-Romeu Odeillo, France

[2] Univ. Grenoble Alpes INES - CEA,
50 avenue Lac Léman, 73375 Le Bourget-du-Lac, France

* Corresponding author. Email: stephane.abanades@promes.cnrs.fr. Phone: + 33 (0)4 68 30 77 30.

ABSTRACT

Several hybridization strategies of a solar-autothermal biomass gasifier were examined for stable and continuous operation under variable solar irradiation. The ultimate objective was to demonstrate the feasibility of controlled syngas production, through the modification of oxygen, water, and biomass injection rates. Various hybridization strategies were probed by thermodynamic analysis and experimentally validated. Thermodynamic equilibrium calculations detailed the impact of both H_2O and O_2 injection rates on the produced syngas composition under constant wood feeding. Oxygen injection decreased the H_2:CO molar ratio, while reducing the solar thermal power required to carry out the gasification reaction. Meanwhile, the total H_2+CO production dropped by 1.36 mole of H_2 and 0.64 mole of CO per mole of O_2 added, independently of the quantity of water provided. Validation experiments were then carried out under real concentrated solar flux in a directly-irradiated conical spouted-bed reactor, following distinct hybridization paths. Maintaining constant the H_2:CO ratio above 1 during hybridization required to provide high amounts of water steam with oxygen, which penalized the gasifier efficient heating. In contrast, minimizing the water injection rate throughout hybridization strongly altered the H_2:CO ratio but decreased the CO_2 production and the solar thermal power requirement. Finally, the successful control of the outlet H_2+CO volume flow rate with simultaneous oxygen and wood injection was demonstrated (under constant water feeding rate). Solar-to-fuel efficiencies were kept around 20%, while hybridization decreased the cold-gas efficiency below 80%.

KEYWORDS

Concentrated solar energy, Solar reactor, Solar fuels, Steam-gasification, Biomass, Solar-autothermal hybridization.

1. INTRODUCTION

The production of solar fuels has become a promising research field in the domain of renewable energies. Upgraded syngas can be synthesized from local biomass and waste resources via pyrolysis

and gasification processes, and it has multiple industrial applications. First of all, its tunable H_2 and CO contents make it an essential raw feedstock in the chemical industry (e.g. the synthesis of biofuels and alcohols). Its enhanced heating value also allows efficient energy storage and combustion for the production of heat and electrical power. In comparison with the direct combustion of solid biomass or waste feedstocks, power production from gasification products allows to reduce the emissions of SO_2 and NO_x by a factor of 10 [1], as the removal of pollutants from a syngas stream is easier than the cleaning of the flue gas emitted from direct biomass combustion. Regarding the integration of carbon capture in power plants, which may become essential in the coming decades, its cost could be halved in integrated gasification combined cycles (IGCC) when compared to processes based on direct biomass combustion [1].

To that extent, a high amount of heat must be provided to gasifiers to cope with the high reaction enthalpy. In conventional plants, oxy-combustion occurs inside the reactor to maintain sufficient temperatures in the reaction zone. Around 75% of the overall biomass energy content is reported to be converted into syngas heating value [2], losses being due to the combustion of feedstock and to thermal losses. The integration of alternative, renewable heat sources has thus been investigated as a way to limit the CO_2 yields and to convert a higher part of the biomass resource, given that biomass is still moderately available in comparison to fossil fuels [3]. As a result, solar gasification processes have been widely investigated in the last decades, as they eliminate the need for partial feedstock combustion for process heat supply and thus allow to increase the biomass utilization rate by 30% [4], through indirect storage of concentrated solar energy providing the reaction enthalpy. These technologies allow to produce a clean syngas, with carbon conversion efficiencies (CCE) exceeding 90%. The cold-gas efficiency (CGE) can reach up to 1.3 [5], which means that the feedstock energy content is upgraded through the solar process. Meanwhile, typical solar-to-fuel efficiencies (SFE) are found between 20-30% [6]. Higher H_2:CO ratios than in conventional processes can also be achieved (1.16 versus 1.07 in [7]), as well as higher syngas yields per unit mass of feedstock and lower CO_2 contents. The integration of solar gasifiers in plants for the poly-generation of power and fuels [8–10] is thus being extensively explored.

Solar gasification, however, implies fluctuating syngas production rates through the daily and yearly variations of the solar resource. Operation during cloudy days, reactor start-up and shut-down must therefore be carefully monitored in order to stabilize the reactor temperature and the syngas quality, and to improve process efficiency [11]. Several ways are available to smooth out the heat availability through high-inertia media, as reviewed in [12]. For instance, the use of an external heat-transfer fluid was studied for coal gasification [13], enabling continuous day-night operation at the cost of a 16-hour heat storage. As an alternative, reactors featuring molten-salt media have been proposed [14] to integrate heat storage into the gasifier itself and thus attenuate solar energy fluctuations. A reactor design featuring a molten-salt medium was developed [15], and coupled with a hybridization method that uses in-situ injection of oxygen [16]. This method, referred as Solar-Autothermal Hybrid Gasification (SAHG) [17], has become a promising solution to achieve continuous solar gasifier operation, as demonstrated experimentally in [18]. Increased temperatures and carbon conversion efficiency were observed when O_2 was injected, at the expense of reduced H_2 yields and thus H_2:CO molar ratios. This effect could be limited by injecting additional H_2O, thanks to the water-gas shift reaction. It was however noticed that increasing the H_2:CO mole ratio from 1.0 to 1.7 required a water flow rate nine times higher than the stoichiometric one [16], thus questioning the actual feasibility of such control. Boujjat et al. also investigated SAHG both experimentally [19] and numerically [20], using a hybridized spouted-bed reactor and eventually proposing an application to solid-recovered fuel gasification [21]. Recent experimental investigations of the hybridized spouted-bed revealed the impact of O_2 injection rate, operating temperature (in the range 1200-1300 °C) and reactor heating mode (direct versus indirect heating of the cavity) [22].

The impact of H_2O and O_2 injection rates is ruled by the set of chemical equations given below, starting with the global reaction of steam gasification (Equation 1). After the pyrolysis of biomass into

gases, tars, and char, the so-called gasification of char occurs (Equation 2) as well as combustion reactions (hydrogen in Equation 3, carbon monoxide in Equation 4, char in Equation 5), water-gas shift equilibrium (Equation 6) and steam-methane reforming (Equation 7). Besides, the impact of reactants flow rates was extensively assessed in the domain of conventional gasification. Regarding the injection of oxygen, typical results showed a significant decrease of the H_2 content and an increase of the CO_2 content due to combustion reactions, which did not systematically come with a decrease of the CO mole fraction [23,24]. The CO content only seemed to decrease at high inlet O_2:C molar ratios [25], which was also pointed out in recent investigations about spouted-bed hybridization [22]. This shows that hydrogen combustion (Equation 3) tends to be favored in comparison with carbon monoxide combustion (Equation 4). In the work of Campoy et al. [26], the impact of oxygen quantity on gases production rates, thermochemical performance and reactor efficiency was also carefully assessed under several steam injection rates.

Beech wood steam gasification:
$CH_{1.66}O_{0.69} + 0.31\ H_2O_{(v)} \rightarrow CO + 1.14\ H_2$ $\Delta H° = +143$ kJ/mol (1)

Char steam gasification:
$C_{(s)} + H_2O_{(g)} \rightarrow H_2 + CO$ $\Delta H° = +131$ kJ/mol (2)

Hydrogen combustion:
$H_2 + ½\ O_2 \rightarrow H_2O_{(l)}$ $\Delta H° = -285$ kJ/mol (3)

Carbon monoxide combustion:
$CO + ½\ O_2 \rightarrow CO_2$ $\Delta H° = -283$ kJ/mol (4)

Char combustion:
$C_{(s)} + O_2 \rightarrow CO_2$ $\Delta H° = -394$ kJ/mol (5)

Water-gas shift equilibrium:
$H_2O + CO \leftrightarrow H_2 + CO_2$ $\Delta H° = -42$ kJ/mol (6)

Steam methane reforming:
$CH_4 + H_2O \rightarrow CO + 3\ H_2$ $\Delta H° = +206$ kJ/mol (7)

The addition of H_2O was extensively discussed as well. Under low injection rates, steam was proven to increase the H_2 production and to decrease the CO production [27,28], according to the water-gas shift reaction (Equation 6). Accordingly, the CO_2 production unavoidably increased with water addition. At higher H_2O injection rates, and depending on the feedstock particles diameter [29], the performance indicators tended to stabilize [30,31] or even decrease after reaching an optimum [26,32]. Optimal H_2+CO, H_2:CO, H_2 mole fraction, syngas LHV, efficiencies and waste deposits were even observed in [33] at a given steam-to-carbon ratio. A compromise must thus be found between syngas upgrade (water addition during hybridization) and thermal performance (water removal). The coupled injection of O_2 and H_2O must thus be carefully planned to reach enhanced performances. In conventional oxygen-steam gasification, the H_2O:O_2 ratio is occasionally stated (order of magnitude 2:1 in [28]), and may be a relevant indicator to find advantageous operating conditions at given temperature and pressure conditions [34].

In this study, further insights were provided into the role of water addition during SAHG. The aim was to compare several strategies of reactants feeding for controlled syngas production during solar hybrid gasification:

- Progressive addition of H_2O during hybridization to control the H_2:CO ratio (path #1);

- Minimization of H_2O injection during hybridization to optimize thermal performance (path #2);
- Progressive addition of biomass feedstock during hybridization to control the H_2+CO production (path #3).

The ultimate objective was to demonstrate the feasibility of continuous syngas production despite a reduction of solar power input in the solar reactor, whilst providing recommendations regarding control design during SAHG. A new approach was therefore proposed at thermodynamic equilibrium to map the evolution of reactor performance as a function of both H_2O and O_2 injection rates. The strategies for gaseous reactants (both O_2 and H_2O) and biomass feedstock injection were experimentally investigated, using a small-scale solar spouted-bed gasifier.

2. MATERIALS AND METHODS

2.1. Directly irradiated spouted-bed gasifier

2.1.1. Experimental setup overview

Solar gasification was performed in a spouted-bed reactor (Figure 1), located at the focal point of a vertical-axis solar furnace. The metallic cavity was made of a highly resistant FeCrAl alloy. It comprised a 68 mm high, 60° cone topped with a cylindrical piece of 78 mm inner diameter and 46 mm height. Down the cone, an injection nozzle enabled the stirring and conversion of solid particles thanks to a mixed flow of argon (0.2 NL/min) and oxidizing agents (H_2O and O_2 flow rate ranging from 0 to 0.5 g/min and 0 to 0.5 NL/min, respectively). Wood injection and syngas recovery were located around the cylindrical region. This region was topped by an alumina cap, which was protected by two layers of zirconia felts (2 mm thick each). A layer (30 mm thick) of insulating material (alumino-silicate fiber boards) was arranged around the cavity, and a transparent Pyrex glass window allowed proper sealing of the reactor. A second protective flow of argon (2 NL/min) was blown towards the window to keep it clean from pyrolytic smokes.

(a)

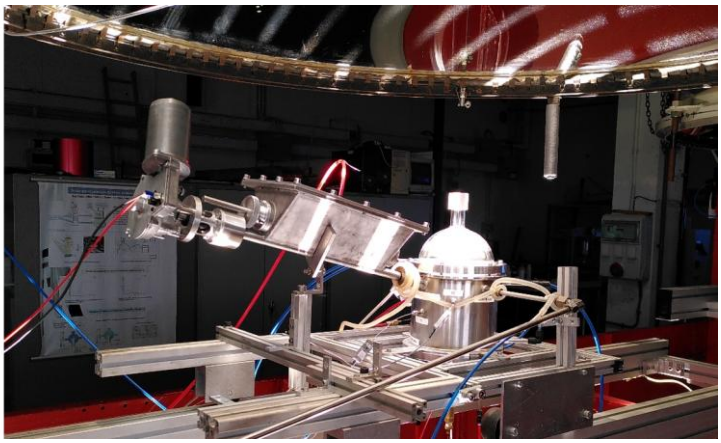

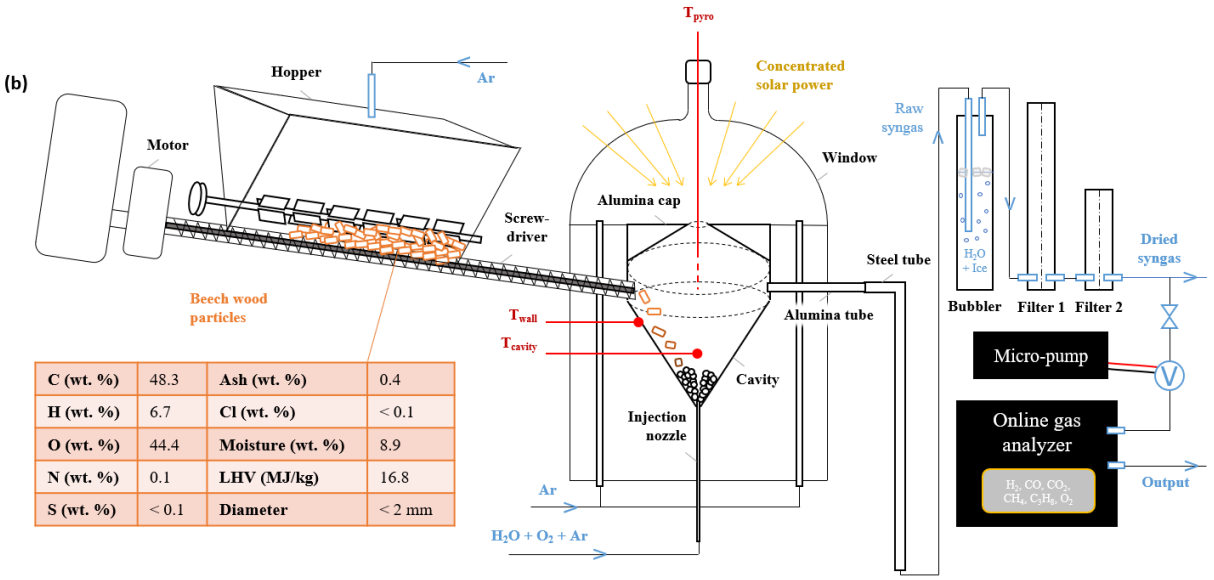

C (wt. %)	48.3	**Ash (wt. %)**	0.4
H (wt. %)	6.7	**Cl (wt. %)**	< 0.1
O (wt. %)	44.4	**Moisture (wt. %)**	8.9
N (wt. %)	0.1	**LHV (MJ/kg)**	16.8
S (wt. %)	< 0.1	**Diameter**	< 2 mm

Figure 1. (a) Photograph of the gasification reactor during solar heating, (b) Scheme of the reactor cavity, wood injection system, and syngas treatment components.

Wood particles were stored in a hopper and fed via a screw driver towards the cavity. The hopper was regularly hit to warrant smooth particles flow (series of eight blows, at least once per minute), and a set of rotating steel fins (serving as arch breaker) could be manually activated to prevent blockage of the feeding. Argon was continuously injected in the hopper (0.5 NL/min), and circulated towards the reactor via the screw path to limit counterflow heat and mass transfer in the feeder.

The gases injection rates were monitored via four mass flow controllers (BROOKS 5850 S). Demineralized liquid water was injected via a stainless-steel capillary inserted inside the injection nozzle, and fed by a liquid mass flow controller (HORIBA SILV-F30P). In total, 2.7 NL/min of argon were injected during heating to empty the reactor from air. The reactants were directly heated by sunlight, concentrated by a parabolic mirror of 2 m diameter. The incoming thermal power was controlled thanks to a shutter obstructer: the correlation between the shutter aperture and the thermal power available at the focal point (named solar power input in the following) was established by calorimetry at different shutter openings under a direct normal irradiance (DNI) of 1000 W/m² (nominal power of 1.5 kW_{th} at full shutter opening).

2.1.2. Output flow, temperature, and pressure measurement devices

The produced syngas was collected via an outlet alumina tube. It flowed through a long steel tube (ensuring a first cooling step), and then through a set including one bubbler (condensation of steam and char deposits) and two micro-filters in series (char deposits). A drying column (DRIERITE desiccant bed) was optionally added between the two filters. Finally, from the output stream, a constant sampling flow (1 NL/min) was pumped and analyzed by an online device (GEIT GAS 3100 SYNGAS). The measurement of H_2, CO, CO_2, CH_4, C_nH_m (calibrated with C_3H_8) and O_2 flow rates was continuously performed, allowing an assessment of the gasifier performances.

Temperatures were measured by B-type thermocouples. One was placed right against the external cavity wall surface, near the top of the conical piece (T_{wall}), and one was shielded with alumina and placed at the center of the spout region (T_{cavity}). A third temperature measurement (T_{pyro}) was enabled thanks to a solar-blind pyrometer (wavelength 4.8-5.2 µm corresponding to a H_2O absorption band), pointing down vertically through a CaF_2 window and towards the cavity bottom. Furthermore, a

pressure measurement was performed right inside the cavity to monitor the proper evacuation of syngas and pumping was performed to maintain this pressure at around 0.87 bar.

2.1.3. Calibration of the wood injection device and reproducibility test

In our previous work [22], it was stated that altered syngas production rates could have been caused by a progressive decrease of the wood injection rate in the reactor. A new effort was thus undertaken to calibrate the screw driver, and provide more stable wood injection rates. It was decided to fill in the hopper with 150 g of wood particles before the beginning of experiments (instead of 30 g or 50 g in previous works), and to stop the injection after the distribution of ~100 g. This way, a stable flow rate of wood (1.2 g/min) could be maintained over more than 80 minutes, with a measured standard deviation of 0.064 g/min. Calibration and reproducibility tests were performed in a cold setup. Then, a dedicated reproducibility gasification experiment was done at 1300 °C (Figure 2, using nitrogen instead of argon with the same volume flow rates). Two consecutive injections of 1.2 g/min of wood and 0.2 g/min of steam were performed, and lasted 20 minutes each. When the reactants were injected, the solar power input was adjusted through the opening of the shutter obstructer, so that the temperature inside the cavity remained at 1300 °C. The temperatures T_{wall} and T_{pyro} were recorded (Figure 2-a), as well as the main gases output flow rates and the solar power input (Figure 2-b). Between these two injection periods, the measured yields of H_2, CO, CO_2, and CH_4 differed by only 2.1%, 1.7%, 0.0%, and 3.4%, respectively. Syngas production was thus stable and results reproducibility was checked. Meanwhile, the average solar power required to maintain the cavity at constant temperature differed by only 1.1% (it equaled successively 1333 and 1348 W). This experimental series thus demonstrated the proper results reproducibility. It further confirmed that the biomass injection protocol is suitably mastered, as well as the temperature control method and the syngas composition measurement.

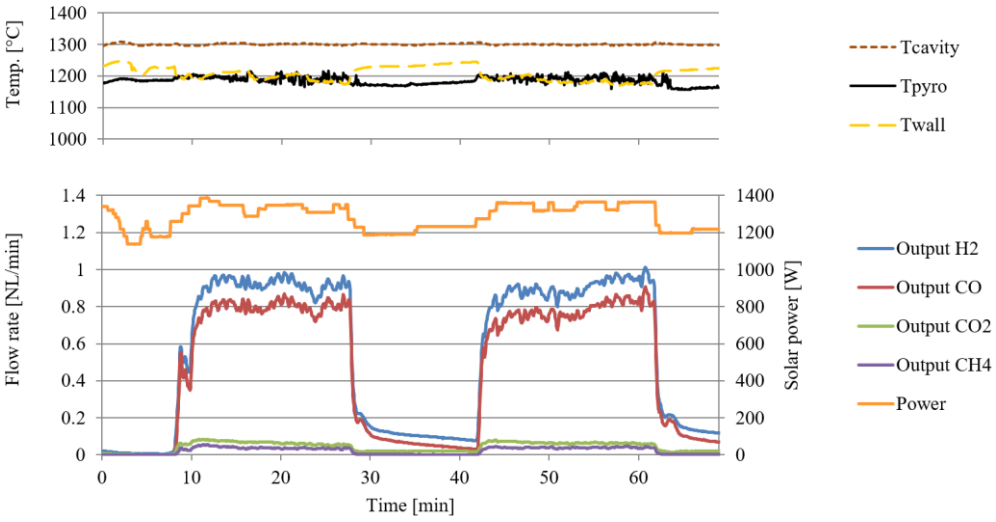

Figure 2. Evolution of (a) reactor temperatures and (b) reactants and products flow rates along with input solar power during two injection periods with identical reactants flow rates (1.2 g/min wood + 0.2 g/min H_2O).

Finally, the calibration of the biomass feeding system was performed under various motor voltages (determining the rotation speed of the screw). Figure 3 shows the evolution of wood flow rates under voltages of 4.9, 7.2, and 9.6 V. In the time intervals delimited by squares, average flow rates of 0.76, 1.18, and 1.72 g/min were achieved, respectively. It was noticed that the higher the voltage, the shorter the duration of stable injection (corresponding approximately in each case to the injection of 100 g) and the higher the standard deviation (that equaled 0.043, 0.064, and 0.098 g/min, respectively).

Thanks to these measurements, the wood injection rate could be suitably mastered during long gasification experiments.

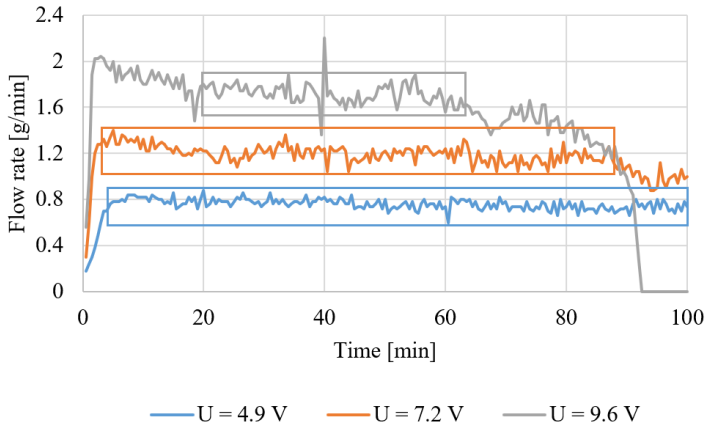

Figure 3. Evolution of wood flow rates under decreasing input voltages to the motor.

2.2. Simulation at thermodynamic equilibrium

Estimation of the reactor products outcome was performed with Python, using the open-source library CANTERA [35]. This library allowed to calculate the composition of multiphasic solid-gas mixtures at thermodynamic equilibrium, by minimizing the Gibbs' free energy at given conditions of temperature and pressure. Thermodynamic properties were taken from CANTERA's database, featuring the GRI-30 data for gases, and the graphite data for solid carbon particles. The same assumption for solid carbon phase was proposed and validated in [36]. The properties of wood were not available in CANTERA's model. Instead, the atoms contained in the wood flow (C, H, O) were provided as $C_{(s)}$, H_2 and O_2 species to account for the initial elemental chemical composition of the system.

In order to estimate the thermal power consumed by the overall reaction, the enthalpy of the reactants injected at room temperature and the enthalpy of the products streams at reactor temperature were calculated. The standard enthalpy of formation of the wood was deduced from its LHV (16.8 MJ/kg), that was measured by calorimetry on a dry basis, and equaled -178.9 kJ/mol. The enthalpy of the products was given by CANTERA at the cavity temperature. The pressure was set to 0.85 atm (atmospheric pressure at reactor location). The simulation of wood gasification at thermodynamic equilibrium could be performed as a function of the wood, H_2O and O_2 injection rates. An injection of argon sweep gas was also set, to account for the power required to heat it from room temperature to the cavity temperature. This mainly impacted the overall thermal power required to carry out the reaction.

3. RESULTS AND DISCUSSION

3.1. Mapping of reactor performances

Thanks to the computational code written with CANTERA, a map of the products composition (Figure 4) was plotted under constant biomass flow rate (1.2 g/min, wet basis) and temperature (1300 °C). The horizontal and vertical axes indicate the injection flow rates of liquid water and oxygen, respectively. The maximal values correspond to the maximal flow rates available in the experimental setup: 0.50

g/min of water (H_2O:C = 0.76 mol/mol) and 0.50 NL/min of oxygen (O_2:C = 0.50 mol/mol). A line (char limit) delimits the zone where char conversion is incomplete. Over the remaining domain, the lines of constant H_2:CO molar ratio are depicted in Figure 4-a. Figure 4-b indicates the power consumed by the overall gasification reaction, based on the enthalpies of reaction computed with CANTERA (the heating of 2.7 NL/min of argon is included). Figure 4-c and Figure 4-d show the production rates of CO_2 and H_2O respectively, and Figure 4-e and Figure 4-f detail the production rates of H_2 and CO respectively.

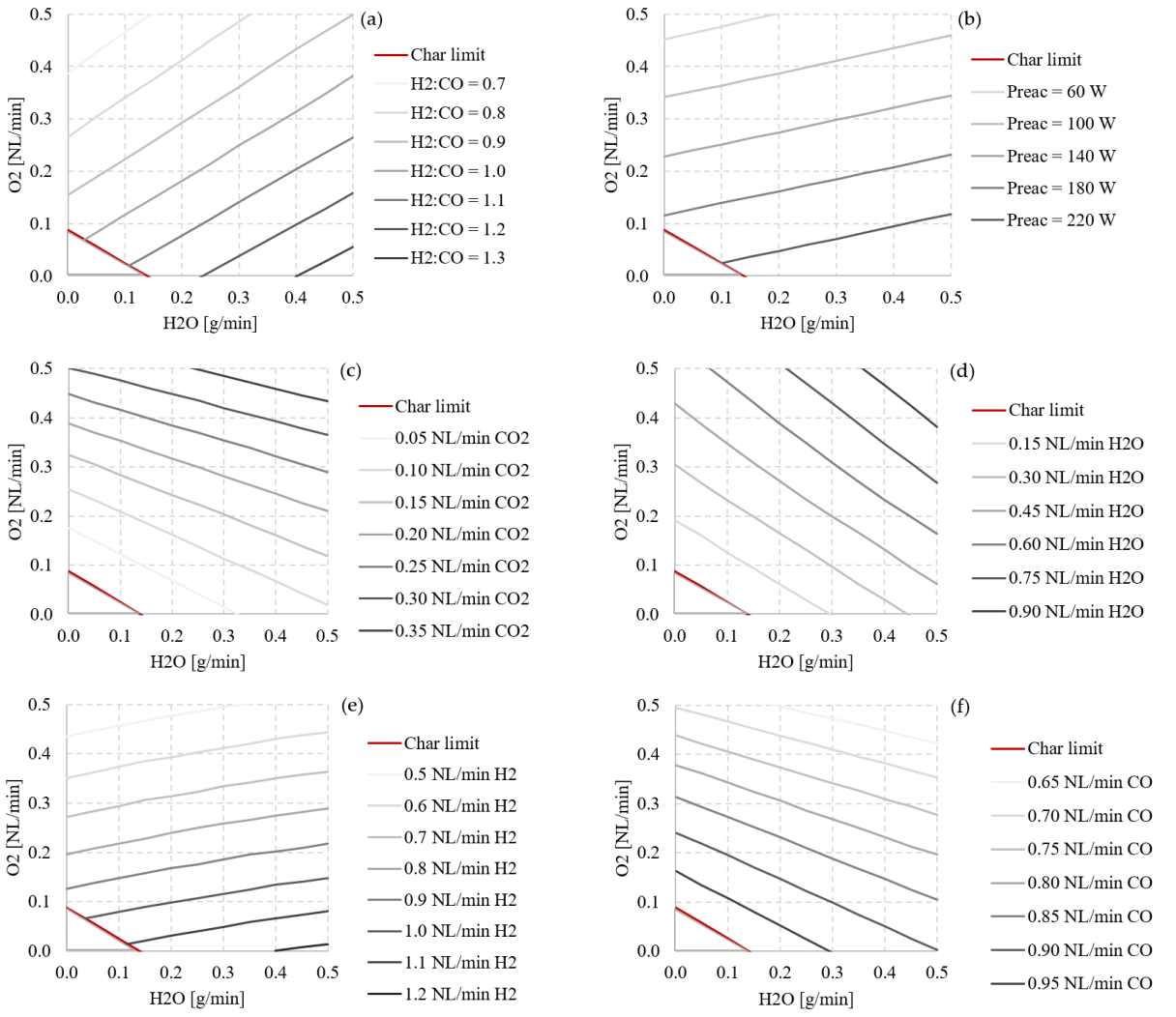

Figure 4. Map of the reactor performances as a function of H_2O and O_2 injection rates, under constant temperature (1300 °C) and wood injection rate (1.2 g/min), according to thermodynamic equilibrium.

Figure 4-a points out that the H_2:CO ratio increases when water is added, and decreases when oxygen is added. The decrease of the H_2:CO ratio is mainly due to the decrease of the H_2 production rate (Figure 4-e), as it is consumed by oxy-combustion in priority. Meanwhile, the entire CO consumed by the addition of oxidants (oxy-combustion or water-gas shift) is converted into CO_2: the variations shown in Figure 4-c and Figure 4-f are almost identical. The increase of the H_2O production rate is caused by both the addition of oxygen (oxy-combustion of H_2) and the injection of supplementary water. Figure 4-c and Figure 4-d also show that, at the limit of full char conversion, neither CO_2 nor H_2O are produced at all. Finally, Figure 4-b confirms that oxygen injection contributes to heat the reactor. The gain reported is found between 35.1 and 36.0 W per 0.1 NL/min of additional O_2 injected. In counterpart, both 0.136 NL/min of H_2 and 0.064 NL/min of CO are lost per 0.1 NL/min of O_2 added (i.e., 2 moles of H_2+CO per mole of O_2).

This set of graphs is a powerful tool to design hybrid control strategies. Indeed, at a given flow rate of O_2, the injection rate of H_2O is a key parameter: reducing it allows to reduce the power required for the reaction (hybrid mode), in association with lower H_2 production, whereas increasing it allows to enhance H_2 production thanks to water-gas shift. Both approaches can be justified, depending on how the reactor is integrated inside a complete process. Besides, it appears that the sum of the H_2 and CO volume flow rates does not depend on the addition of water, as seen in Figure 5. Between 0.0 NL/min and 0.5 NL/min of oxygen injected, the H_2+CO volume flow rate decreases from 2.12 to 1.12 NL/min, showing that an addition of feedstock is required to maintain a constant H_2+CO production. The injection of water in the gasifier just aims at maintaining a given H_2:CO ratio at the exit of the reactor, at the cost of additional thermal power requirements.

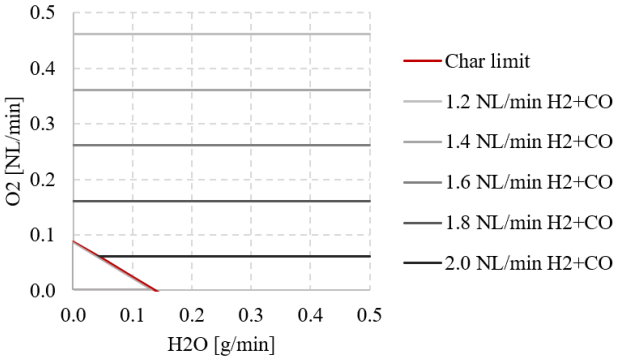

Figure 5. Map of the summed H_2 and CO volume flow rates as a function of H_2O and O_2 injection rates, under a constant temperature (1300 °C) and wood injection rate (1.2 g/min), according to thermodynamic equilibrium.

3.2. Allothermal-hybrid gasification under different steam flow rates

The experimental validation of hybrid gasification strategies was carried out under a fixed cavity temperature. To overcome DNI variations and changes in reactants flow rates, the shutter obstructer was continuously monitored to control the solar power input entering the reactor cavity. Thus, T_{cavity} remained at 1300 °C ± 10 °C (like in Figure 2). This temperature was chosen based on a previous study showing improved performance compared to 1200 °C [22,37]. A record of the shutter aperture was kept, so the solar power input could be deduced at each instant (time-step of 3 s) and averaged over gasification periods.

The hybridization of the spouted-bed gasifier by injecting oxygen and additional wood was already investigated in previous studies [19,22,38]. They showed a reactor cavity temperature maintained above 1300 °C, while the solar power input decreased by about 40% (from 1200 W to 700 W). In counterpart, the H_2:CO molar ratio dropped below 1, the global syngas production was altered and the CO_2 production rate was multiplied by 3. As stated previously [22], this decline of syngas production was partly due to decreasing wood injection rates with time. To tackle this issue, the experiment under direct solar heating was carried out again with the newly calibrated screw driver setup. The reactants flow rates are given in Table 1: injections #A and #B correspond to allothermal and hybrid gasification cases, and injections #C and #D are attempts to control the H_2 production thanks to water steam addition. The Equivalence Ratio (ER, defined in Equation 8) during hybrid gasification equals 5.21. The durations of wood injection periods are given in Table 1 as well, not including ramp-up periods. Results are provided in Figure 6 (time evolution curves) and Figure 7 (bar charts with standard deviations).

$$ER = (n_{biomass}/n_{O2})/(n_{biomass}/n_{O2})_{combustion\ stoichiometry} \quad (8)$$

Along this series, the cavity temperature was successfully maintained at 1300 °C despite varying injection rates of reactants. In Figure 6, T_{cavity} remained between 1288 and 1312 °C during the entire allothermal-hybrid gasification run, with a standard deviation of 4.1 °C. Steady injection periods were characterized by plateauing temperature curves, and significant variations of T_{cavity} only occurred right after the changes of reactants flow rates. These changes also contributed to modify T_{wall} and T_{pyro} values because of a different heating source: from full-solar to combustion-aided heating, the temperature of the reactor walls tended to decrease whereas temperature of the gas phase in the spout region was drastically increased. Finally, during steady operation, the input solar power kept on oscillating because of slightly varying wood injection flow rates.

Table 1. Reactants flow rates during allothermal-hybrid gasification.

Injection #	Input H_2O [g/min]	Input O_2 [NL/min]	Input wood [g/min]	Duration [min]
A	0.2	0.00	1.2	12.7
B	0.2	0.25	1.45	18.9
C	0.3	0.25	1.45	7.4
D	0.4	0.25	1.45	7.4

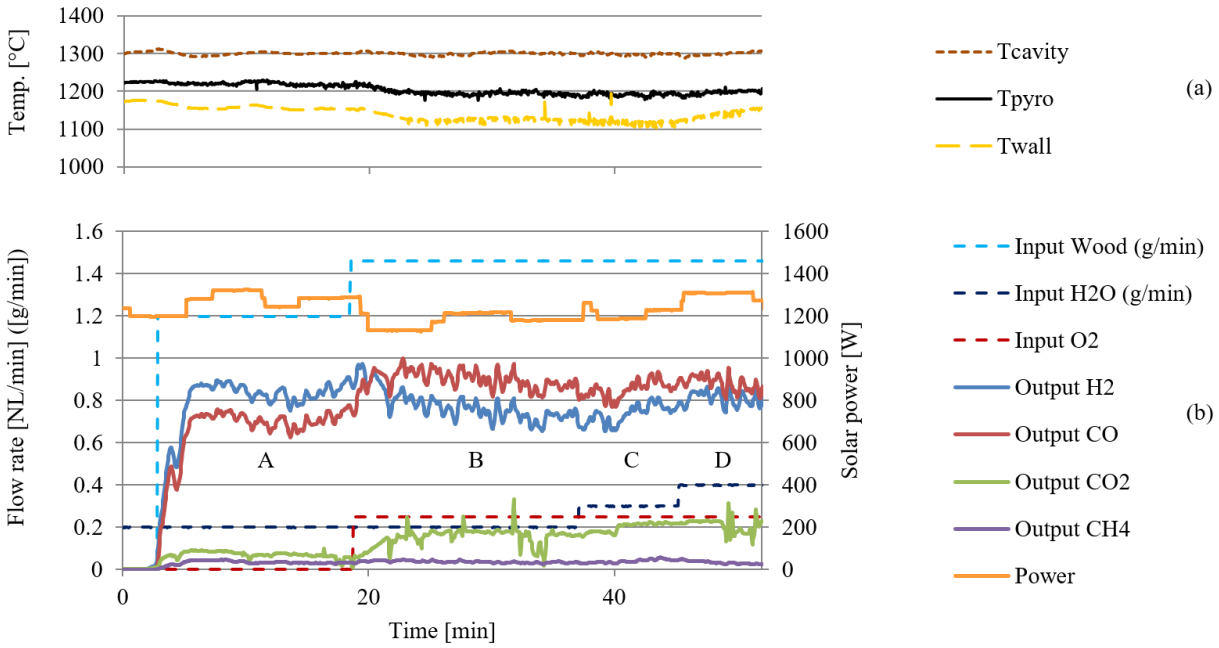

Figure 6. Evolution of (a) reactor temperatures and (b) reactants and products flow rates along with input solar power during allothermal-hybrid gasification (see Table 1).

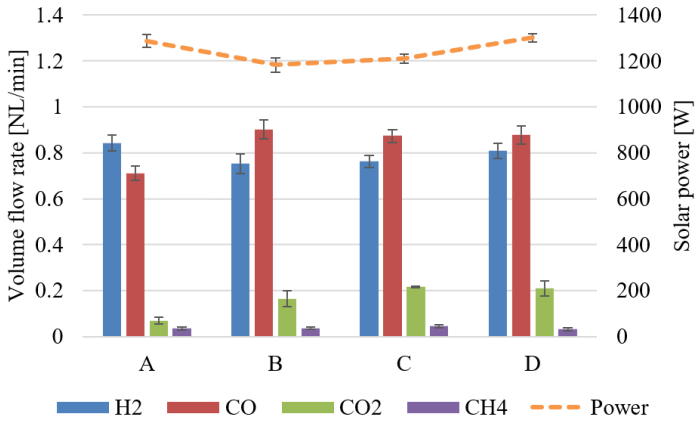

Figure 7. Averaged products flow rates and input solar power during allothermal-hybrid gasification.

During injection #A, only wood (1.2 g/min) and water (0.2 g/min) were provided. The output flow rates of H_2 and CO quickly reached 0.84 and 0.71 NL/min, while small productions of CO_2 and CH_4 were settled (0.07 and 0.04 NL/min, respectively). Then, during injection #B, oxygen (0.25 NL/min) was added along with a supplemental flow of wood (0.25 g/min). Oxy-combustion led to an increase of the mean CO_2 production rate (reaching 0.16 NL/min), but decent production rates of H_2 and CO were maintained thanks to the addition of wood. Even though the H_2:CO ratio was decreased below 1 (decreasing from 1.19 during allothermal to 0.84 during hybrid operation), the sum of the H_2 and CO flow rates remained equal to 1.6 NL/min. Meanwhile, the averaged solar power input was decreased from 1290 to 1180 W thanks to in-situ combustion: this gain was lower than the one reported in previous studies, because the quantity of wood injected was well maintained to its setpoint flow rate. The temperature of the reactor wall decreased with oxygen injection, because direct solar heating was partly replaced with in-situ oxy-combustion, directly heating the reaction volume.

During the last two injections (injection #C and #D), the water flow rate was increased (to 0.3 and 0.4 g/min) to improve the H_2:CO ratio again despite hybridization. This resulted in an increase of the H_2 production rate (from 0.75 NL/min during injection #B to 0.81 NL/min during injection #D), but it was insufficient to reach a H_2:CO ratio above 1. More water should have been injected, but water addition tended to highly penalize the thermal performance of the reactor. At a certain point, hybrid gasification did not allow to reduce the solar power input anymore. Similar thermal powers were required between injections #A and #D (1300 W and 1290 W respectively) to keep the cavity temperature at 1300°C, while thermodynamic equilibrium showed that a 40 W gain was possible between those operating points. In other words, the decrease of the temperature caused by a reduction of solar power input could not be compensated by the addition of O_2.

The mismatch between syngas composition control (through additional injection of H_2O) and proper heating of the reactor, which was already shown in Figure 4, was therefore clearly illustrated. This path consisting of the addition of steam while maintaining constant both oxygen and biomass injection rates (denoted as path #0 in the following) enabled to increase the production of H_2, but was unsuitable to operate under a reduced solar power input during SAHG.

3.3. Theoretical impact of water injection rates throughout solar-autothermal hybridization

The allothermal-hybrid runs studied above highlighted the need to find a compromise between syngas quality and thermal performances. Thermal power is consumed to heat and vaporize the provided

water, making the reactor heating less efficient. On the contrary, low water injection rates may enable improved thermal performance at the cost of an altered syngas quality. Distinct hybridization strategies were designed using the diagram given in Figure 4-a. Depending on whether the H_2:CO ratio was to be controlled or not, several paths could be drawn, starting from allothermal gasification (1.2 g/min wood and 0.2 g/min water) and following various trajectories with O_2 addition. Two paths are detailed below and illustrated in Table 2:

- In path #1, the water input flow rate was increased along with O_2 injection flow rate to follow a line of constant H_2:CO ratio, in order to stabilize the syngas composition;
- In path #2, the water input flow rate was minimized while O_2 was injected, to reduce the quantity of reactants required and ensure more efficient heating.

Table 2. Description of two hybridization paths in the diagram of Figure 4-a.

	Illustration	Path goal
Path #1	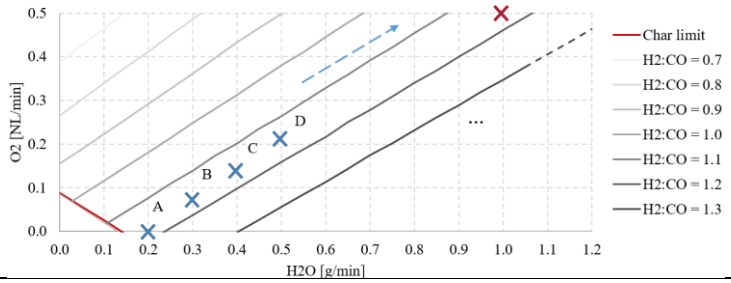	Control the quality of syngas at all costs
Path #2	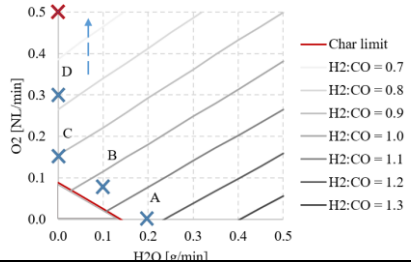	Minimize the quantity of water injected

A calculation case was computed at thermodynamic equilibrium, under a 1.2 g/min flow rate of biomass, to assess the performances of both hybridization strategies. In Table 3, the point corresponding to allothermal gasification (injection #A) was compared with the points corresponding to hybrid gasification with a 0.5 NL/min flow rate of O_2 (red crosses in Table 2). This flow rate of O_2 is the maximal one reachable with the experimental setup. It corresponds to an ER of 2.15 (feedstock injection rate of 1.2 g/min). Following path #1, 1.02 g/min of water must be injected in addition to the 0.5 NL/min of O_2 to maintain the H_2:CO ratio to the value of allothermal gasification (1.18 mol/mol). This results in higher H_2 and CO productions than following path #2, at the expense of higher CO_2 production (0.48 NL/min instead of 0.30 NL/min) and output steam flow rate (1.62 NL/min instead of 0.53 NL/min). Water injection in path #1 significantly increases the steam concentration inside the reactor, facilitating the char gasification over its partial combustion and favoring the water-gas shift reaction (Equation 6), even if only a small fraction of H_2O is actually consumed by the overall reaction. The heating and evaporation of water however drain heat, so the total power required to reach thermodynamic equilibrium at 1300 °C is higher in path #1 (129 W) than in path #2 (43 W). Both values are found below the one required during allothermal gasification (237 W), thanks to the heat provided by oxy-combustion inside the reactor. Besides, the LHV of the produced dry syngas is divided by two between allothermal and hybrid gasification (8.0 MJ/kg following path #1 and 9.0 MJ/kg following path #2, instead of 18.2 MJ/kg during allothermal gasification). The choice of an

optimization strategy therefore impacts the H_2:CO ratio much more than the LHV of the produced syngas.

Table 3. Theoretical outcomes of paths #1 and #2, under constant biomass flow rate (1.2 g/min), compared with allothermal operation, all calculated at thermodynamic equilibrium.

	Allothermal gasification	Path #1, 0.5 NL/min O_2	Path #2, 0.5 NL/min O_2
Water injected [g/min]	0.2	1.02	0.0
H_2 production [NL/min]	1.15	0.61 (-47%)	0.43 (-63%)
CO production [NL/min]	0.98	0.52 (-47%)	0.70 (-29%)
CO_2 production [NL/min]	0.02	0.48	0.30
Steam output [NL/min]	0.06	1.62	0.53
H_2:CO ratio [mol/mol]	1.18	1.18	0.62
Syngas LHV (dry) [MJ/kg]	18.2	8.0	9.0
Power required [W]	237	129 (-46%)	43 (-82%)

3.4. Experimental validation of increased or minimized water injection rates throughout solar-autothermal hybridization

This section deals with the control strategies of paths #1 and #2. For each one of them, four conditions of reactants injection were performed under constant wood flow rate (1.2 g/min). Each injection period lasted between 15 and 20 minutes, in order to properly reach steady state and to limit the uncertainty linked to the variations of solar power input. Between the injection periods, oxidants were still provided until the H_2 and CO flow rates decreased back to quasi-null values (to ascertain that char was totally consumed). The results from the first injection of path #1, which characterize the reference case of allothermal steam gasification, were used as the first injection of path #2. All the oxidants flow rates are given in Table 4. The main results are summarized in Figure 8 (time evolution curves following path #1), Figure 9 (time evolution curves following path #2), and Figure 10 (bar charts with standard deviations).

Table 4. Reactants flow rates during paths #1 and #2.

	Path #1				**Path #2**			
Injection #	Input wood [g/min]	Input H_2O [g/min]	Input O_2 [NL/min]	Duration [min]	Input wood [g/min]	Input H_2O [g/min]	Input O_2 [NL/min]	Duration [min]
A	1.2	0.2	0.00	14.2	1.2	0.2	0.00	14.2
B	1.2	0.3	0.08	17.6	1.2	0.1	0.08	13.8
C	1.2	0.4	0.15	17.1	1.2	0.0	0.15	15.4
D	1.2	0.5	0.23	16.9	1.2	0.0	0.30	16.1

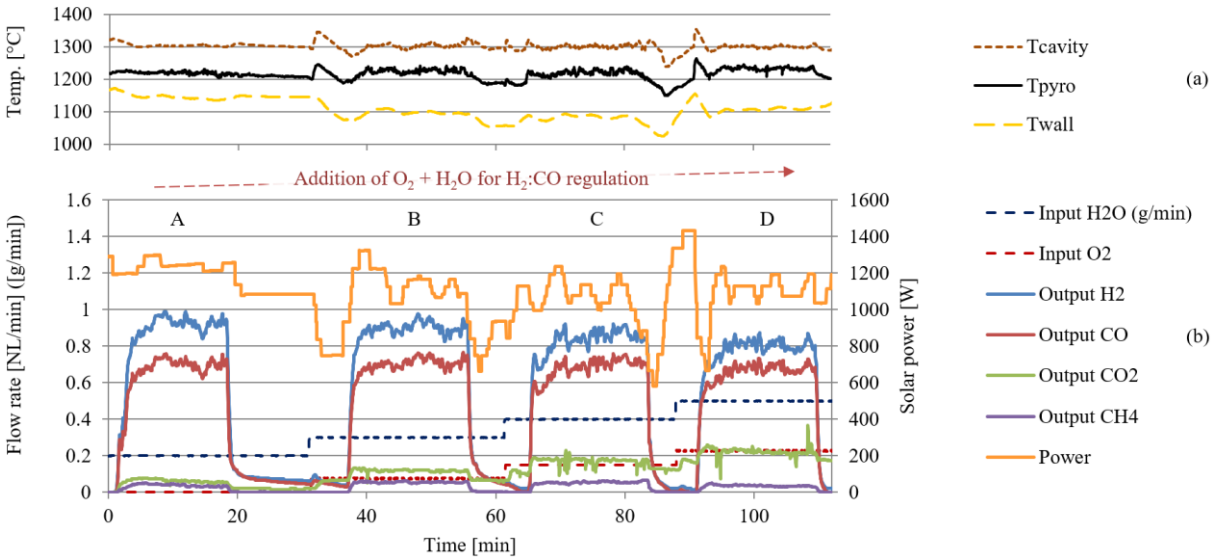

Figure 8. Evolution of (a) reactor temperatures and (b) reactants and products flow rates along with input solar power during gasification with controlled H_2:CO ratio (path #1, see Table 4).

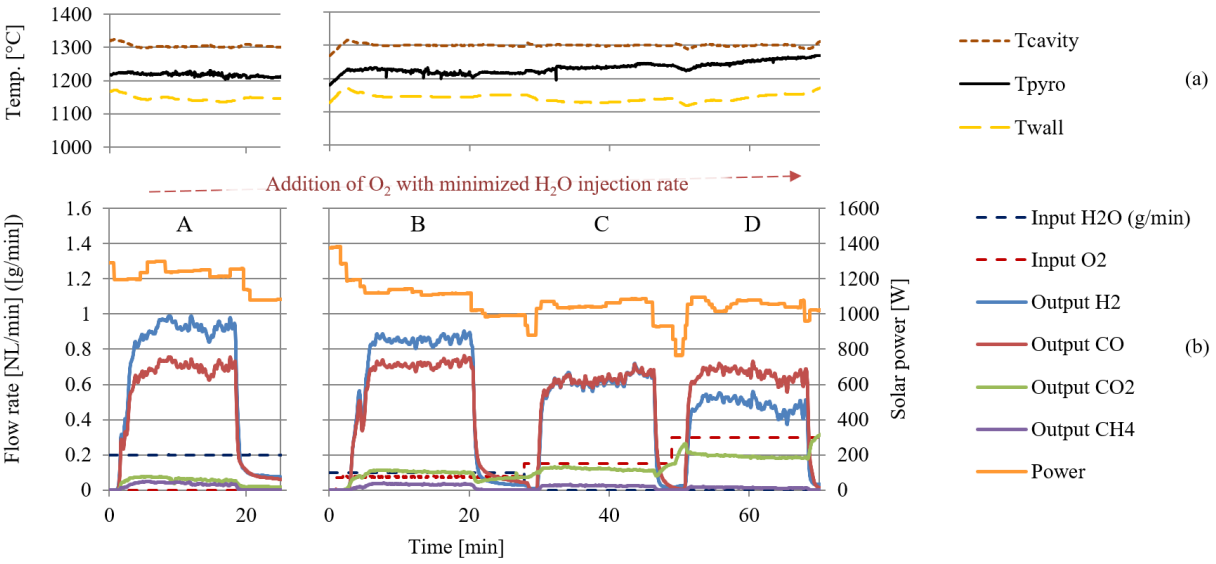

Figure 9. Evolution of (a) reactor temperatures and (b) reactants and products flow rates along with input solar power during gasification with minimized H_2O injection rate (path #2, see Table 4).

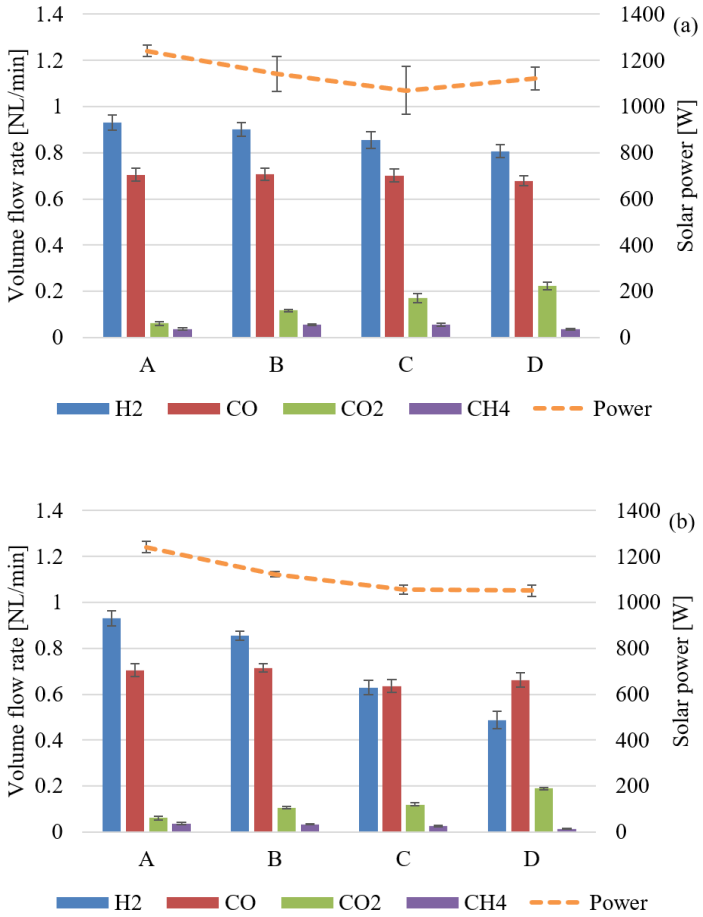

Figure 10. Averaged products flow rates and input solar power following (a) path #1 and (b) path #2.

Path #1 aimed to maintain the H_2:CO ratio constant while increasing both H_2O and O_2 injection rates. Figure 10-a shows that, by following path #1, the H_2:CO ratio could be maintained above 1 despite oxygen injection. The ER for injections #B to #D was respectively 13.5, 7.18, and 4.68. The averaged H_2 flow rate only decreased from 0.93 to 0.81 NL/min between injection #A and #D. Meanwhile, the averaged CO_2 flow rate increased from 0.06 to 0.22 NL/min because of oxy-combustion occurring inside the reactor. These attractive results, however, came with low thermal benefit: a gain of ~100 W in the required solar power input was observed between injections #A and #B, and then no significant decrease of the required solar power (to maintain the temperature at 1300°C) was noticed between injections #B and #D (Figure 10-a). The data available for injection #C suffered from a high uncertainty, as difficulties were encountered to properly maintain T_{cavity} at 1300 °C. As the power produced by combustion was partly consumed by the water evaporation and heating, controlling the H_2:CO ratio directly inside the reactor via steam addition did not seem to be promising enough in such conditions. Thermodynamics indeed showed that the exothermal reaction of water-gas shift (Equation 6) favored the production of H_2 only at low temperatures (< 800 °C) [39], which explains why such high quantities of water had to be provided at 1300 °C.

In Figure 9 (path #2), opposite trends are exhibited. Indeed, path #2 consisted in increasing the O_2 injection while decreasing steam for more efficient heating at the expense of lower H_2:CO ratio. The ER for injections #B to #D was respectively 13.5, 7.18, and 3.59. When oxygen was injected, the H_2 flow rate consistently decreased from 0.93 to 0.49 NL/min. As a result, the H_2:CO ratio dropped from 1.32 to 0.74. The productions of CO_2 were lower than the ones observed following path #1 because of lower H_2O injection rates (0.19 NL/min of CO_2 emitted for 0.30 NL/min of O_2 injected versus 0.22 NL/min of CO_2 for 0.23 NL/min of O_2 injected in path #1). Meanwhile, a steadier decrease of the

required solar power for maintaining the cavity temperature constant was observed, especially between injections #A, #B, and #C. The gain reached ~190 W (Figure 10-b), which was favored by the reduction of the water injection rate. The gain between injections #C and #D was less significant, because no decrease of the water flow rate occurred (input H_2O flow rate was zero in both conditions). The interest of minimizing the H_2O injection rate was thus demonstrated in terms of thermal performance (i.e., decrease of the required solar power for operation at a constant temperature) and CO_2 emissions, but it came with a drastic decrease of both the hydrogen production and the H_2:CO ratio.

3.5. Adjustment of both oxygen and wood injection rates under constant steam flow rate

In the previous section, it was shown that a decrease of the H_2:CO ratio would occur during hybridization unless high quantities of water are provided. The decrease of hydrogen production might thus be compensated by increasing the wood injection rate, even though the H_2:CO ratio keeps on decreasing because of oxy-combustion. An adjustment of the wood feeding rate upon increasing oxygen flow rate was therefore performed while the water injection rate was maintained constant (Table 5). This strategy was denoted as path #3. It differed from path #0, in which water was increasingly added while both O_2 and biomass were kept constant. It also differed from paths #1 and #2, as these did not feature varying biomass feeding rates. Based on thermodynamic calculations, the wood and O_2 input flow rates were chosen to maintain the H_2+CO volume flow rate constant (in the range 1.11-1.13 NL/min), while the water injection rate always equaled 0.1 g/min. This way, high-enough amounts of gas were supposed to be available to achieve a constant production of both H_2 and CO thanks to a downstream water-gas shift unit. The calorific value of the syngas, given as the power available by burning the output flow, was also kept stable (in the range 215-222 W), because of similar H_2 and CO molar lower heating values (Equations 3 and 4).

To achieve the objective stated above, the wood feeding rate was increased from 0.63 to 1.2 g/min while the O_2 flow rate was increased from 0.0 to 0.5 NL/min. The inlet O_2:C molar ratios were comparable to those studied in [22], as they reached 0.50 mol/mol for injection #F. The ER for injections #B to #F was respectively 10.5, 5.39, 3.59, 2.69, and 2.15. Six conditions of reactants injection each lasting between 10 and 12 minutes were performed consecutively, without any interruption between each other. The obtained time evolution curves of output gases flow rates and solar power input are provided in Figure 11. The measured temperatures are provided as well, showing particularly high values for T_{pyro} at high O_2:C ratios, when compared with previous series due to the more pronounced effect of combustion.

Table 5. Reactants flow rates and thermodynamic equilibrium predictions during gasification with controlled H_2+CO volume flow rate (path #3).

Injection #	Input H_2O [g/min]	Input O_2 [NL/min]	Input wood [g/min]	Duration [min]	Output H_2 [NL/min]	Output CO [NL/min]	H_2+CO [NL/min]	Gas combustion power [W]
A	0.1	0.00	0.63	9.6	0.60	0.51	1.11	215
B	0.1	0.06	0.70	10.8	0.57	0.54	1.11	217
C	0.1	0.13	0.78	11.4	0.55	0.57	1.12	218
D	0.1	0.22	0.88	12.2	0.51	0.60	1.11	219
E	0.1	0.34	1.02	10.0	0.49	0.64	1.13	221
F	0.1	0.50	1.20	10.3	0.45	0.67	1.12	222

The averaged H_2, CO, CO_2, and CH_4 volume flow rates are plotted in Figure 12, as well as the solar power input required for each injection condition. The productions estimated at thermodynamic equilibrium are shown as well for the sake of comparison. This revealed that the H_2 and CO outcomes were overestimated at low injection rates, while the CO_2 production rate was perfectly predicted. The standard deviation of both the output flow rates and the solar power recordings were rather low, as the very progressive variations of the injection rates made the control of temperature easier.

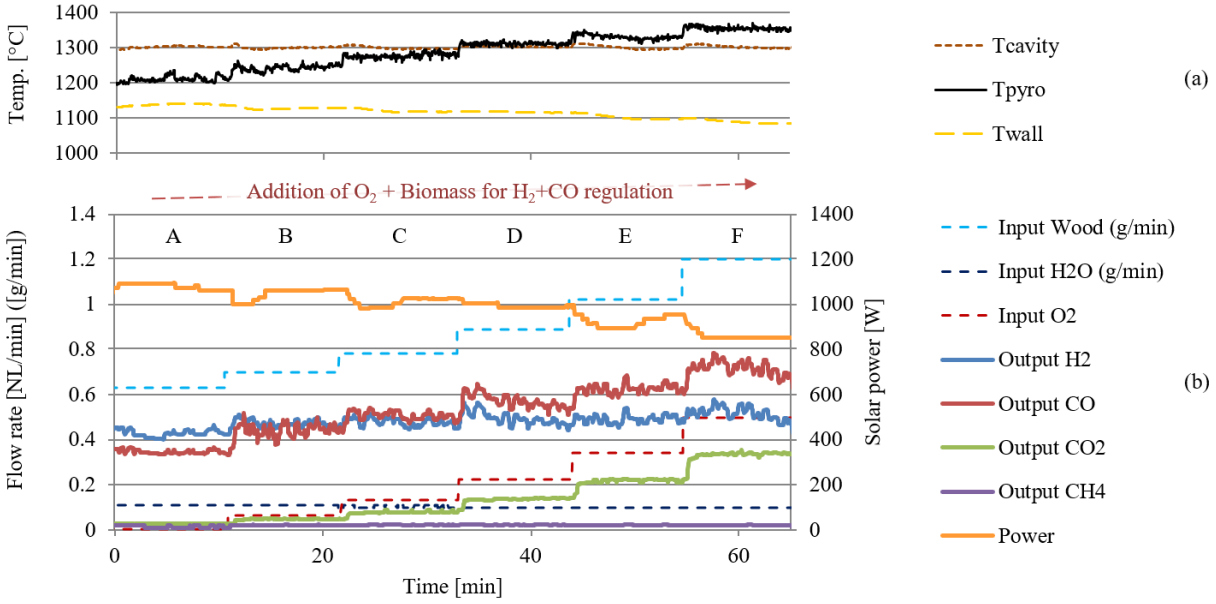

Figure 11. Evolution of (a) reactor temperatures and (b) reactants and products flow rates along with input solar power during gasification with controlled H_2+CO volume flow rate (path #3, see Table 5).

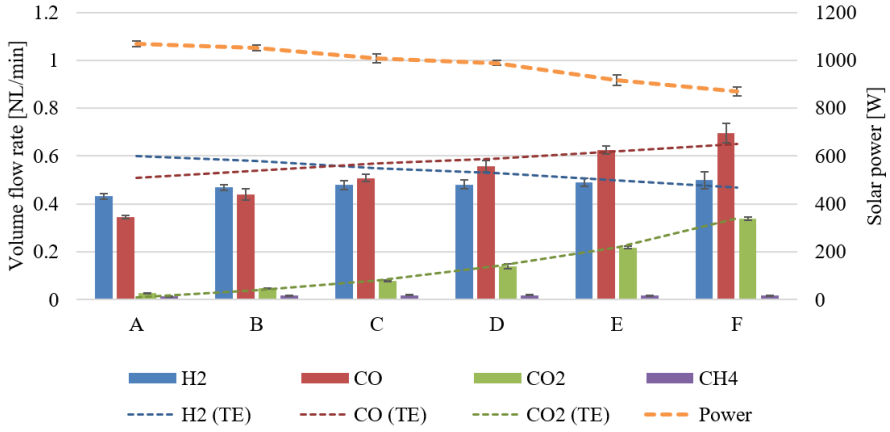

Figure 12. Averaged products flow rates, thermodynamic equilibrium predictions, and input solar power during gasification with controlled H_2+CO volume flow rate (path #3).

As expected, the H_2:CO ratio decreased during hybridization (from 1.25 to 0.72). As observed in Figure 11, the CO production increased strongly (rising from 0.34 to 0.70 NL/min) thanks to the addition of wood, and so did the CO_2 production because of injected O_2. Meanwhile, the H_2 production rate remained between 0.40 and 0.58 NL/min, while following a slight increase. As a result, the sum of H_2 and CO volume flow rates did not decrease during hybridization as it did in paths #1 and #2. Its average value even increased despite oxygen injection, from 0.78 to 1.20 NL/min (Figure 12). This unexpected growth was caused by a gap between thermodynamic equilibrium modelling and experimental results, especially under low wood feeding rates. Indeed, the overall

conversion of wood is favored by high input flow rates [40], as it enables the formation of a thick-enough bed of solid particles and thus a better circulation within the reactor and an efficient absorption of heat. Through a better prediction of the reactor outcome, which would imply further modelling of the reactor hydrodynamics, the H_2+CO production rate could hence be properly controlled despite oxygen injection.

Meanwhile, it was observed that the solar power required to maintain a constant cavity temperature decreased gradually. A total gain of 200 W was reported between injections #A and #F, with values decreasing from 1070 to 870 W (injection #F: conversion of 1.2 g/min of wood aided by 0.5 NL/min of O_2). Such results were promising, as they proved that the adjustment of the wood injection rate during hybridization was compatible with an efficient and progressive heating of the reactor cavity. Therefore, hybridization based on a dynamic control of wood and oxygen injection must be feasible in a combustion-aided hybrid solar gasifier, without seeking to maintain a constant H_2:CO ratio [41]. Both the total syngas output (sum of H_2 and CO flow rates) and the syngas calorific value (power available from syngas combustion) can be maintained constant throughout the day.

3.6. Overview of thermochemical performance trends

Three main thermochemical performance indicators were determined [21]. The carbon-conversion efficiency (CCE, Equation 9) quantifies the fraction of carbon atoms (contained in wood feedstock) converted into syngas components (mainly CO, CO_2, and CH_4). C_2H_m species were not included in the calculation, which may lead to slightly underestimate the CCE values. This efficiency still reached values above 90% in certain cases, when high enough oxidizing agents were injected. The cold-gas efficiency (CGE, Equation 10) is the ratio between the energy output (cold syngas) and the energy input (feedstock). As in the CCE calculation, C_2H_m hydrocarbons were not considered. Thus, due to the high heating values of these hydrocarbons, the CGE was underestimated by up to 12% [31]. Finally, the solar-to-fuel efficiency (SFE, Equation 11) was assessed based on the energy content of cold biomass and syngas, as well as the solar energy absorbed by the reactor during gasification.

$$CCE = \frac{C_{syngas}}{C_{feedstock}} = \frac{n_{CO}+n_{CO_2}+n_{CH_4}}{n_{CH_{1.66}O_{0.69}}} \quad (9)$$

$$CGE = \frac{LHV_{syngas}\cdot m_{syngas}}{LHV_{feedstock}\cdot m_{feedstock}} = \frac{LHV_{H_2}\cdot m_{H_2}+LHV_{CO}\cdot m_{CO}+LHV_{CH_4}\cdot m_{CH_4}}{LHV_{CH_{1.66}O_{0.69}}\cdot m_{CH_{1.66}O_{0.69}}} \quad (10)$$

$$SFE = \frac{LHV_{syngas}\cdot m_{syngas}}{Q_{solar}+LHV_{feedstock}\cdot m_{feedstock}} = \frac{LHV_{H_2}\cdot m_{H_2}+LHV_{CO}\cdot m_{CO}+LHV_{CH_4}\cdot m_{CH_4}}{Q_{solar}+LHV_{CH_{1.66}O_{0.69}}\cdot m_{CH_{1.66}O_{0.69}}} \quad (11)$$

In these three efficiency calculations, the considered dry wood molecules were represented by the raw formula $CH_{1.66}O_{0.69}$ (Equation 1). The masses m_i indicate the total masses (kg) of reactants injected during gasification, or the masses of products measured during the same periods. The LHV_i values are given in J/kg. Finally, Q_{solar} indicates the solar energy (in J) that entered the reactor during the gasification period. The solar energy input at thermal equilibrium (steady-state temperature) is dispatched into the useful energy available for the gasification reaction (including reactants heating and reaction enthalpy) and thermal losses. For instance, in the case of solar gasification (allothermal) of 1.2 g/min of biomass at 1300°C, the solar energy input was 1.31 MJ, and 21% of this input was used for the reaction as useful energy. The remaining corresponded to thermal losses including radiative, conductive and convective heat losses (a representative energy loss distribution was detailed in [20]).

An overview of the performance assessment is provided in Figure 13. In the four graphs corresponding to the four allothermal-hybrid series (paths #0, #1, #2, and #3), efficiencies are provided for each injection condition. The values of the CCE ranged between 0.64 and 0.93. They tended to increase with the addition of oxidants in the reactor. Because of limiting kinetics, the more H_2O and O_2 were injected, the better the biomass was converted. The lowest values were obtained during allothermal gasification, under 1.2 g/min of wood and 0.2 g/min of H_2O (CCE = 0.68, injection A of paths #1 and #2) or under 0.63 g/min of wood and 0.1 g/min of H_2O (CCE = 0.64 , injection A of path #3).

CGE values ranged between 0.69 and 1.00, and tended to decrease with high O_2 flow rates. In Figure 13-b, Figure 13-c, and Figure 13-d, they reached 0.9 and then systematically decreased after injection #B. The CGE did not go below 0.8 following path #1, thanks to the gradual injection of water to maintain a constant H_2:CO ratio. It, however, decreased below 0.7 following paths #2 and #3 because of downgraded syngas quality: at a biomass flow rate of 1.2 g/min, similar values were found at 0.0 g/min of H_2O + 0.3 g/min of O_2 (CGE = 0.69), and at 0.1 g/min of H_2O + 0.5 g/min of O_2 (CGE = 0.70).

Finally, the SFE values varied around 20%, even if slightly lower values were found at low wood injection rates. A higher SFE value means a better utilization of the solar energy and biomass resources to produce a given amount of syngas. Accordingly in Figure 13-d, the CGE decreased because of the injection of oxygen whereas the SFE increased as the biomass injection rate increased, thus denoting a higher solar energy conversion into products. A minimal SFE value of 13% was found during the allothermal gasification of 0.63 g/min of wood (injection #A of path #3), because of an under-utilization of the solar reactor capacity. This result raised the issue of reactor dimensioning: a strategy such as the one followed in path #3, with lower biomass injection rates during allothermal gasification than during hybrid gasification, could impeach the optimal exploitation of the available solar power because of insufficient injection rates of wood. In path #2, a gradual decrease of the SFE from 19% to 16% was also noticed because of reduced H_2O injection rates, which shows the interest of not totally stopping water injection during hybridization for global performance purpose.

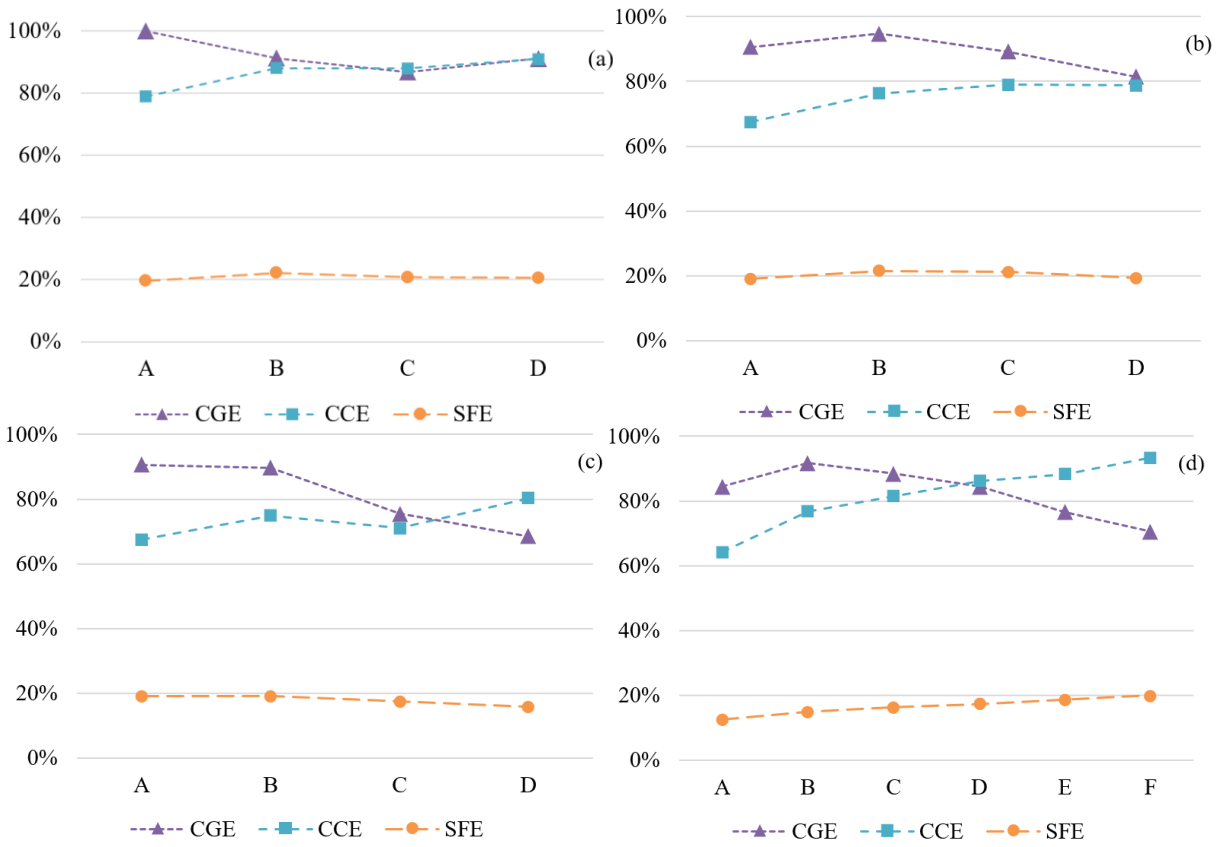

Figure 13. Thermochemical reactor efficiencies during solar allothermal-hybrid operation following: (a) path #0, (b) path #1, (c) path #2, and (d) path #3 gasification series.

4. CONCLUSION

The operational feasibility of the solar biomass conversion process through partial oxy-combustion of the feedstock to control the gasification temperature was studied. The control of a spouted-bed SAHG reactor under decreasing solar power was done following different hybridization strategies:

- The mere addition of oxygen (0.25 NL/min) and wood (0.25 g/min) allowed to compensate for a solar power decrease from 1290 to 1180 W during hybridization (-8.5%), while maintaining a SFE higher than 20% and a CGE higher than 90% (path #0).
- Supplemental addition of water during hybridization enabled to control the H_2:CO molar ratio inside the reactor, but could be detrimental because of a higher solar power demand, important biomass and H_2O resource requirements, and elevated CO_2 production rates (path #0 and path #1).
- Contrarily, minimizing the water injection rate resulted in an efficient reactor heating, counterbalanced by a drop of the H_2:CO ratio from 1.32 to 0.74 and a gradual decrease of both the CGE and the SFE (path #2). The solar power required to maintain the cavity at 1300 °C decreased from 1240 to 1050 W (-15.3%, at 0.3 NL/min of O_2 injected), while it decreased from 1240 to 1120 W (-9.7%, at 0.23 NL/min of O_2 injected) when the H_2:CO ratio was maintained constant.

- Finally, it was shown that increasing both biomass and oxygen feeding rates under constant steam input was suitable to prevent the decrease of the syngas production output (H_2+CO volume flow-rate) due to in-situ combustion (path #3). Increasing H_2 and CO productions were even observed, and a 200 W gain was reported (from 1070 to 870 W, -18.7%, at 0.5 NL/min of O_2 injected) regarding the solar power input required to maintain the cavity temperature at 1300 °C. The increase of the wood injection rate was therefore compatible with a performant heating of the gasifier during hybridization.

Hybrid gasification is thus useful for achieving stable process operation upon fluctuating solar power input. In-situ water-gas shift via steam addition is still hardly viable, when compared with a strategy aiming at maintaining a constant H_2+CO production (leaving the control of H_2:CO ratio to a downflow shift unit), or a constant syngas calorific value (i.e. constant available power from syngas combustion).

These experimental results were obtained with a small-scale reactor. Thermochemical performances reported here can thus be hardly extrapolated towards industrial scale. Still, the results on syngas composition can be further exploited (e.g. design of new kinetic models for hybridized gasifiers), as they cover a wide range of H_2O and O_2 injection rates. They confirm that spouted-bed reactors are good candidates for SAHG, as they can operate under both solar and combustion-aided heating. They can accommodate hybrid operation over a wide range of biomass, water and oxygen input flow rates, which is attractive for the development of efficient hybridization strategies applied to solar thermochemical gasification processes.

NOMENCLATURE

Abbreviations

- CCE Carbon Conversion Efficiency
- CGE Cold-Gas Efficiency
- DNI Direct Normal Irradiance (W/m²)
- IGCC Integrated Gasification Combined Cycle
- LHV Lower Heating Value (J/kg)
- SAHG Solar-Autothermal Hybrid Gasification
- SFE Solar-to-Fuel Efficiency
- TE Thermodynamic Equilibrium

Physical variables

- C_i Molar amount of carbon atoms in species i
- $\Delta H°$ Standard enthalpy of reaction (J/mol)
- LHV_i Lower heating value of species i (J/kg)
- m_i Mass of the species i produced or consumed during gasification (kg)
- n_i Molar amount of species i produced or consumed during gasification
- Q_{solar} Solar energy received during gasification (J)

DECLARATION OF COMPETING INTEREST

The authors declare that they have no known competing financial interests or personal relationships that could have appeared to influence the work reported in this paper.

ACKNOWLEDGEMENTS

This work received partial funding from the European Union's Horizon 2020 research and innovation programme under grant agreement No 823802 (project SFERA-III), along with financial support from

CEA (French Alternative Energy and Atomic Energy Commission) and Région Occitanie for the PhD grant of A. Curcio.

REFERENCES

[1] P. Basu, Biomass gasification and pyrolysis: practical design and theory, Academic Press, Academic Press, Burlington, MA, 2010.

[2] P. McKendry, Energy production from biomass (part 3): gasification technologies, Bioresource Technology. 83 (2002) 55–63. https://doi.org/10.1016/S0960-8524(01)00120-1.

[3] G.J. Nathan, M. Jafarian, B.B. Dally, W.L. Saw, P.J. Ashman, E. Hu, A. Steinfeld, Solar thermal hybrids for combustion power plant: A growing opportunity, Progress in Energy and Combustion Science. 64 (2018) 4–28. https://doi.org/10.1016/j.pecs.2017.08.002.

[4] Y. Fang, M.C. Paul, S. Varjani, X. Li, Y.-K. Park, S. You, Concentrated solar thermochemical gasification of biomass: Principles, applications, and development, Renewable and Sustainable Energy Reviews. 150 (2021) 111484. https://doi.org/10.1016/j.rser.2021.111484.

[5] S. Abanades, S. Rodat, H. Boujjat, Solar Thermochemical Green Fuels Production: A Review of Biomass Pyro-Gasification, Solar Reactor Concepts and Modelling Methods, Energies. 14 (2021) 1494. https://doi.org/10.3390/en14051494.

[6] D. Yadav, R. Banerjee, A review of solar thermochemical processes, Renewable and Sustainable Energy Reviews. 54 (2016) 497–532. https://doi.org/10.1016/j.rser.2015.10.026.

[7] M. Kruesi, Z.R. Jovanovic, E.C. dos Santos, H.C. Yoon, A. Steinfeld, Solar-driven steam-based gasification of sugarcane bagasse in a combined drop-tube and fixed-bed reactor – Thermodynamic, kinetic, and experimental analyses, Biomass and Bioenergy. 52 (2013) 173–183. https://doi.org/10.1016/j.biombioe.2013.03.003.

[8] A.A. Kaniyal, P.J. van Eyk, G.J. Nathan, P.J. Ashman, J.J. Pincus, Polygeneration of Liquid Fuels and Electricity by the Atmospheric Pressure Hybrid Solar Gasification of Coal, Energy Fuels. 27 (2013) 3538–3555. https://doi.org/10.1021/ef400198v.

[9] Z. Bai, Q. Liu, J. Lei, H. Li, H. Jin, A polygeneration system for the methanol production and the power generation with the solar–biomass thermal gasification, Energy Conversion and Management. 102 (2015) 190–201. https://doi.org/10.1016/j.enconman.2015.02.031.

[10] W. Saw, A. Kaniyal, P. van Eyk, G. Nathan, P. Ashman, Solar Hybridized Coal-to-liquids via Gasification in Australia: Techno-economic Assessment, Energy Procedia. 69 (2015) 1819–1827. https://doi.org/10.1016/j.egypro.2015.03.158.

[11] J. Petrasch, P. Osch, A. Steinfeld, Dynamics and control of solar thermochemical reactors, Chemical Engineering Journal. 145 (2009) 362–370. https://doi.org/10.1016/j.cej.2008.07.051.

[12] S. Rodat, S. Abanades, H. Boujjat, S. Chuayboon, On the path toward day and night continuous solar high temperature thermochemical processes: A review, Renewable and Sustainable Energy Reviews. 132 (2020) 110061. https://doi.org/10.1016/j.rser.2020.110061.

[13] A.P. Bruckner, Continuous duty solar coal gasification system using molten slag and direct-contact heat exchange, Solar Energy. 34 (1985) 239–247. https://doi.org/10.1016/0038-092X(85)90061-1.

[14] J. Matsunami, S. Yoshida, Y. Oku, O. Yokota, Y. Tamaura, M. Kitamura, Coal gasification by CO_2 gas bubbling in molten salt for solar/fossil energy hybridization, Solar Energy. 68(3) 2000 257-261, . DOI: 10.1016/S0038-092X(99)00074-2

[15] B.J. Hathaway, J.H. Davidson, D.B. Kittelson, Solar Gasification of Biomass: Kinetics of Pyrolysis and Steam Gasification in Molten Salt, Journal of Solar Energy Engineering. 133 (2011) 021011. https://doi.org/10.1115/1.4003680.

[16] B.J. Hathaway, J.H. Davidson, Autothermal hybridization and controlled production of hydrogen-rich syngas in a molten salt solar gasifier, International Journal of Hydrogen Energy. 46 (2021) 15257–15267. https://doi.org/10.1016/j.ijhydene.2021.02.048.

[17] X. Li, Y. Shen, X. Kan, T.K. Hardiman, Y. Dai, C.-H. Wang, Thermodynamic assessment of a solar/autothermal hybrid gasification CCHP system with an indirectly radiative reactor, Energy. 142 (2018) 201–214. https://doi.org/10.1016/j.energy.2017.09.149.

[18] A.P. Muroyama, I. Guscetti, G.L. Schieber, S. Haussener, P.G. Loutzenhiser, Design and demonstration of a prototype 1.5 kWth hybrid solar/autothermal steam gasifier, Fuel. 211 (2018) 331–340. https://doi.org/10.1016/j.fuel.2017.09.059.
[19] H. Boujjat, S. Rodat, S. Chuayboon, S. Abanades, Experimental and numerical study of a directly irradiated hybrid solar/combustion spouted bed reactor for continuous steam gasification of biomass, Energy. 189 (2019) 116118. https://doi.org/10.1016/j.energy.2019.116118.
[20] H. Boujjat, S. Rodat, S. Chuayboon, S. Abanades, Numerical simulation of reactive gas-particle flow in a solar jet spouted bed reactor for continuous biomass gasification, International Journal of Heat and Mass Transfer. 144 (2019) 118572. https://doi.org/10.1016/j.ijheatmasstransfer.2019.118572.
[21] H. Boujjat, S. Rodat, S. Abanades, Solar-hybrid Thermochemical Gasification of Wood Particles and Solid Recovered Fuel in a Continuously-Fed Prototype Reactor, Energies. 13 (2020) 5217. https://doi.org/10.3390/en13195217.
[22] A. Curcio, S. Rodat, V. Vuillerme, S. Abanades, Experimental assessment of woody biomass gasification in a hybridized solar powered reactor featuring direct and indirect heating modes, International Journal of Hydrogen Energy. 46 (2021) 37192–37207. https://doi.org/10.1016/j.ijhydene.2021.09.008.
[23] C.C. Sreejith, C. Muraleedharan, P. Arun, Air–steam gasification of biomass in fluidized bed with CO2 absorption: A kinetic model for performance prediction, Fuel Processing Technology. 130 (2015) 197–207. https://doi.org/10.1016/j.fuproc.2014.09.040.
[24] N.M. Nguyen, F. Alobaid, J. May, J. Peters, B. Epple, Experimental study on steam gasification of torrefied woodchips in a bubbling fluidized bed reactor, Energy. 202 (2020) 117744. https://doi.org/10.1016/j.energy.2020.117744.
[25] J. Zhou, Q. Chen, H. Zhao, X. Cao, Q. Mei, Z. Luo, K. Cen, Biomass–oxygen gasification in a high-temperature entrained-flow gasifier, Biotechnology Advances. 27 (2009) 606–611. https://doi.org/10.1016/j.biotechadv.2009.04.011.
[26] M. Campoy, A. Gómez-Barea, F.B. Vidal, P. Ollero, Air–steam gasification of biomass in a fluidised bed: Process optimisation by enriched air, Fuel Processing Technology. 90 (2009) 677–685. https://doi.org/10.1016/j.fuproc.2008.12.007.
[27] P.M. Lv, Z.H. Xiong, J. Chang, C.Z. Wu, Y. Chen, J.X. Zhu, An experimental study on biomass air–steam gasification in a fluidized bed, Bioresource Technology. 95 (2004) 95–101. https://doi.org/10.1016/j.biortech.2004.02.003.
[28] L.H. Yang, X. Zhang, S. Liu, Underground Coal Gasification Using Oxygen and Steam, Energy Sources, Part A: Recovery, Utilization, and Environmental Effects. 31 (2009) 1883–1892. https://doi.org/10.1080/15567030802462531.
[29] S. Fremaux, S.-M. Beheshti, H. Ghassemi, R. Shahsavan-Markadeh, An experimental study on hydrogen-rich gas production via steam gasification of biomass in a research-scale fluidized bed, Energy Conversion and Management. 91 (2015) 427–432. https://doi.org/10.1016/j.enconman.2014.12.048.
[30] C. Franco, F. Pinto, I. Gulyurtlu, I. Cabrita, The study of reactions influencing the biomass steam gasification processq, (2003) 8.
[31] S. Chuayboon, S. Abanades, S. Rodat, Comprehensive performance assessment of a continuous solar-driven biomass gasifier, Fuel Processing Technology. 182 (2018) 1–14. https://doi.org/10.1016/j.fuproc.2018.10.016.
[32] N. Cerone, F. Zimbardi, L. Contuzzi, M. Prestipino, M.O. Carnevale, V. Valerio, Air-steam and oxy-steam gasification of hydrolytic residues from biorefinery, Fuel Processing Technology. 167 (2017) 451–461. https://doi.org/10.1016/j.fuproc.2017.07.027.
[33] D.S. Upadhyay, K.R. Panchal, A.K.V. Sakhiya, R.N. Patel, Air-Steam gasification of lignite in a fixed bed gasifier: Influence of steam to lignite ratio on performance of downdraft gasifier, Energy. 211 (2020) 118187. https://doi.org/10.1016/j.energy.2020.118187.
[34] M. Arabloo, A. Bahadori, M.M. Ghiasi, M. Lee, A. Abbas, S. Zendehboudi, A novel modeling approach to optimize oxygen–steam ratios in coal gasification process, Fuel. 153 (2015) 1–5. https://doi.org/10.1016/j.fuel.2015.02.083.
[35] D.G. Goodwin, H.K. Moffat, R.L. Speth, Cantera: an Object-oriented Software Toolkit for Chemical Kinetics, Thermodynamics, and Transport Processes, 2021.

[36] M. Baratieri, P. Baggio, L. Fiori, M. Grigiante, Biomass as an energy source: Thermodynamic constraints on the performance of the conversion process, Bioresource Technology. 99 (2008) 7063–7073. https://doi.org/10.1016/j.biortech.2008.01.006.
[37] H. Boujjat, S. Rodat, S. Chuayboon, S. Abanades, Experimental and CFD investigation of inert bed materials effects in a high-temperature conical cavity-type reactor for continuous solar-driven steam gasification of biomass, Chemical Engineering Science. 228 (2020) 115970. DOI: 10.1016/j.ces.2020.115970.
[38] H. Boujjat, S. Rodat, S. Abanades, Techno-economic assessment of solar-driven steam gasification of biomass for large-scale hydrogen production, Processes. 9(3) (2021) 462. https://doi.org/10.3390/pr9030462.
[39] S. Kern, C. Pfeifer, H. Hofbauer, Reactivity tests of the water–gas shift reaction on fresh and used fluidized bed materials from industrial DFB biomass gasifiers, Biomass and Bioenergy. 55 (2013) 227–233. https://doi.org/10.1016/j.biombioe.2013.02.001.
[40] S. Chuayboon, S. Abanades, S. Rodat, Insights into the influence of biomass feedstock type, particle size and feeding rate on thermochemical performances of a continuous solar gasification reactor, Renewable Energy. 130 (2019) 360–370. https://doi.org/10.1016/j.renene.2018.06.065.
[41] H. Boujjat, G.M. Yuki Junior, S. Rodat, S. Abanades, Dynamic simulation and control of solar biomass gasification for hydrogen-rich syngas production during allothermal and hybrid solar/autothermal operation, International Journal of Hydrogen Energy. 45 (2020) 25827–25837. https://doi.org/10.1016/j.ijhydene.2020.01.072.